HHS Public Access

Author manuscript

Nano Res. Author manuscript; available in PMC 2023 December 14.

Published in final edited form as:

Nano Res. 2023 January ; 16(1): 1009–1020. doi:10.1007/s12274-022-4846-9.

In vivo tumor ultrasound-switchable fluorescence imaging via intravenous injections of size-controlled thermosensitive nanoparticles

Liqin Ren[1,2,#], **Yang Liu**[1,2,#], **Tingfeng Yao**[1,2], **Kytai T. Nguyen**[2,3], **Baohong Yuan**[1,2,*]

[1]Ultrasound and Optical Imaging Laboratory, Department of Bioengineering, the University of Texas at Arlington, Arlington, TX 76019, USA

[2]Joint Biomedical Engineering Program, the University of Texas at Arlington and the University of Texas Southwestern Medical Center, Dallas, TX 75390, USA

[3]Department of Bioengineering, the University of Texas at Arlington, Arlington, TX 76019, USA

Abstract

Near-infrared fluorescence imaging has emerged as a noninvasive, inexpensive, and ionizing-radiation-free monitoring tool for assessing tumor growth and treatment efficacy. In particular, ultrasound switchable fluorescence (USF) imaging has been explored with improved imaging sensitivity and spatial resolution in centimeter-deep tissues. This study achieved size control of polymer-based and indocyanine green (ICG) encapsulated USF contrast agents, capable of accumulating at the tumor after intravenous injections. These nanoprobes varied in size from 58 nm to 321 nm. The bioimaging profiles demonstrated that the proposed nanoparticles can efficiently eliminate the background light from normal tissue and show a tumor-specific fluorescence enhancement in the BxPC-3 tumor-bearing mice models possibly via the enhanced permeability and retention effect. *In vivo* tumor USF imaging further proved that these nanoprobes can effectively be switched 'ON' with enhanced fluorescence in response to a focused ultrasound stimulation in the tumor microenvironment, contributing to the high-resolution USF images. Therefore, our findings suggest that ICG-encapsulated nanoparticles are good candidates for USF imaging of tumors in living animals, indicating their great potential in optical tumor imaging in deep tissue.

Graphical Abstract

*Corresponding author: baohong@uta.edu.
#These authors contributed equally to this work.

Ethics approval

All animal studies were approved and regulated by the University of Texas at Arlington's Institutional Animal Care and Use Committee.

Electronic Supplementary Material

Supplementary material (switch-ON/OFF and stability tests, interpolated 2D USF images, and biodistribution results) is available in the online version of this article at http://dx.doi.org/10.1007/

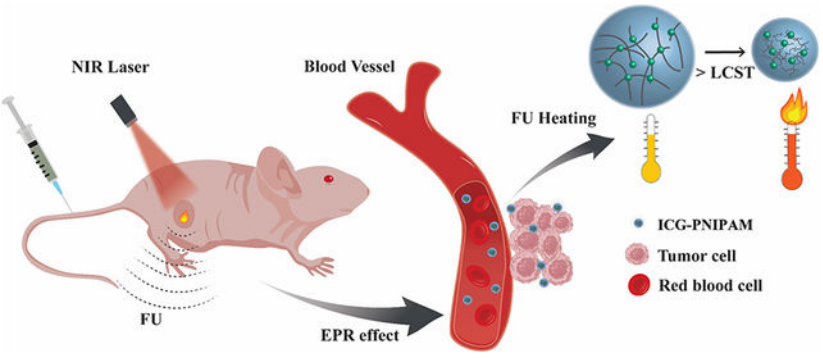

Schematic illustration of temperature-sensitive ICG-PNIPAM nanoprobes showing enhanced fluorescence emission in tumor when FU simulation is applied.

Keywords

in vivo tumor imaging; deep tissue near-infrared (NIR) imaging; high resolution; ultrasound-switchable fluorescence imaging; indocyanine green (ICG)

1 Introduction

Cancer is one of the most common causes of premature death worldwide [1]. In the United States, there are roughly 1,898,160 new cancer cases, and 608,570 individuals died of cancer disease in 2021 [2]. Biomedical imaging plays an essential role in the early detection and characterization of cancers while they are growing. Optical imaging is simple to use and cost-effective compared with alternative imaging techniques such as computed tomography and magnetic resonance imaging. Compared with visible light, fluorescence imaging in the near-infrared (NIR) window (650–900 nm) has several advantages, including deep tissue penetration due to reduced light absorption and scattering, low autofluorescence and background, and therefore high sensitivity and specificity to the adopted fluorophores [3]. Indocyanine green (ICG) is a near-infrared fluorescence dye approved for clinical applications in the United States by the Food and Drug Administration [4]. ICG is often used for sentinel lymph node mapping due to the increased quantum yield (>3 folds) and reduced aggregation from the ICG-protein binding [5]. In addition, ICG molecules can be exploited to image solid tumors (such as hepatocellular carcinoma, liver metastases, and breast tumors) because ICG molecules can passively accumulate into tumor sites via newly formed, porous, and permeable blood vessels [6].

Nevertheless, NIR fluorescence imaging has a poor spatial resolution (~5 mm) in tissues at a depth of centimeters, which hinders the clinical applications of ICG-based fluorescence imaging. Ultrasound-switchable fluorescence (USF) imaging, which combines a fluorescence imaging system with a focused ultrasound (FU) system, has overcome this issue. During USF imaging, the FU pulse causes a temperature increase within the ultrasound focal volume and leads to an increased fluorescence intensity from the temperature-sensitive imaging probes in the confined zone. In this way, the background fluorescent signals from the surroundings can be suppressed. Thus, USF can achieve

acoustic resolution with a fluorescent contrast, which is much higher than optical resolution in deep tissues. Previous studies demonstrated successful USF imaging of sub-millimeter silicone tubes in 3.5 cm and 5.5 cm-thick chicken breast tissues. These promising results proved the applications of USF imaging in centimeter-deep tissues with a high imaging resolution [7-8].

ICG-based poly(N-isopropylacrylamide) (PNIPAM) nanoparticle as one of the USF contrast agents exhibited adjustable lower critical solution temperature (LCST), high stability in biological environments and long shelf-life (>6 months) [9]. *In vivo* USF imaging of mouse organs, such as the spleen and liver, via intravenous (i.v.) injections of PNIPAM nanoparticles was successfully achieved [10]. However, *in vivo* tumor USF imaging via i.v. injections is much more challenging because a sufficient number of nanoparticles must be accumulated in the tumor to achieve an acceptable USF signal-to-noise ratio (SNR). Therefore, local intratumoral injections were usually adopted in our previous studies to bypass this challenge and allow us to focus on addressing other more fundamental and technical challenges [7, 10-12]. With success in the development of various sensitive USF imaging systems and stable contrast agents, *in vivo* tumor USF imaging via i.v. injections has become increasingly more desirable and achievable. In this study, we showed that this goal was achieved by appropriately controlling the size and concentration of ICG-encapsulated PNIPAM (ICG-PNIPAM) nanoparticles. We investigated the size effect of ICG-PNIPAM on USF imaging and tumor accumulation by changing the quantity of surfactants added during the synthesis. Passive tumor targeting of ICG-PNIPAM was demonstrated in BxPC-3 xenograft tumor models with a tumor/normal tissue (T/N) ratio of ~2.3 ± 0.6 at 24 h post-injection. These results indicate that the ICG-PNIPAM nanoparticles are feasible for *in vivo* USF imaging in BxPC-3 tumor, possibly via the enhanced permeability and retention (EPR) effect.

2 Experimental

2.1 Preparation of ICG-PNIPAM nanoparticles

A similar synthesis method of ICG-encapsulated PNIPAM nanoparticles was adopted from our previous publication with modifications [9]. In brief, 1.166 g of N-Isopropylacrylamide (NIPAM) (monomer, 97 %), 0.118 g of acrylamide (AAm) (adjust LCST, ≥99 %), and 12.05 mg of N, N'-methylenebisacrylamide (BIS) (cross-linker, ≥99.5 %) were dissolved in 45 mL deionized (DI) water in a Schleck reaction tube. Various quantities (20 mg, 40 mg, 100 mg, and 200 mg of sodium dodecyl sulfate (SDS) (surfactant, ≥98.5 %) were added into the tube to control the size of the nanoparticles. The mixture was purged with nitrogen gas (99 %, Airgas, USA) for 1 h, stirring at 450 rpm. Then, the ICG (3.54 mg) was quickly poured into the tube, and a rubber stopper was used to seal the tube. Three vacuum/nitrogen purge cycles were conducted to ensure a nitrogen-rich environment. Next, the reaction tube was placed into a 70 °C oil bath, and heated with stirring for 30 min. The 4-4'-Azobis (4-cyanopentanoic acid) (ACA) solution, which was prepared by dissolving 70 mg of ACA (initiator, ≥98 %) into 5 mL of water (pH 10.5), was quickly injected into the reaction tube. The reaction was reacted for 19 h with stirring at 400 rpm. The obtained ICG-PNIPAM nanoparticles were then dialyzed with a dialysis

tube (50 kDa, Spectrum Chemical Mfg. Corp., USA) for 3 days. All chemicals were purchased from Milliporesigma. Samples of PNIPAM nanoparticles are identified using the format: PNIPAM-XmgSDS. "X" represents the quantity of SDS. For example, PNIPAM nanoparticles synthesized with 20 mg SDS is identified as PNIPAM-20mgSDS. Freeze-drying was followed, and the desired concentration of ICG-PNIPAM nanoparticles was prepared by dissolving the freeze-dried samples into DI water. The final concentrations of PNIPAM-20mgSDS, PNIPAM-40mgSDS, PNIPAM-100mgSDS, and PNIPAM-200mgSDS were 79 mg/ml, 88 mg/ml, 80 mg/ml, and 85 mg/ml, respectively. In this study, we adopted the following rule to prepare the final sample solutions: the volume ratio of the final solution to the solution before freeze-drying remained 1/5. Because each sample may have slightly different volume before the freeze-drying, the final concentrations may be slightly different. All final samples were stored at 4 °C in dark.

2.2 Size and zeta potential measurement

The DLS (NanoBrook 90PlusPALS, Brookhaven Instruments, USA) was utilized to measure the hydrodynamic size of PNIPAM nanoparticles. The sample suspension was diluted 30 times (the concentrations of PNIPAM-20mgSDS, PNIPAM-40mgSDS, PNIPAM-100mgSDS, and PNIPAM-200mgSDS were 2.63 mg/ml, 2.93 mg/ml, 2.67 mg/ml, and 2.83 mg/ml, respectively) from the final concentration (as stated in Section 2.1) with DI water in a 3.5 mL quartz cuvette and mixed thoroughly to avoid aggregation before measuring. The measurements were conducted at room temperature and repeated at least 3 times.

The zeta potential of the ICG-PNIPAM nanoparticles was measured by diluting the nanoparticles 30 times from the final concentration with DI water and loading it into a 3.5 mL gold electrode cuvette. Then, the phase analysis light scattering (PALS) (NanoBrook 90Plus PALS, Brookhaven Instruments, USA) was used to conduct zeta potential measurements at room temperature. Each measurement was repeated 5 times.

TEM (H-9500, Hitachi, Japan) was used to study the morphology of ICG-PNIPAM nanoparticles. First, the sample was diluted 50 times from the final concentration with DI water, and the concentrations of PNIPAM-20mgSDS, PNIPAM-40mgSDS, PNIPAM-100mgSDS, and PNIPAM-200mgSDS were 1.58 mg/ml, 1.76 mg/ml, 1.60 mg/ml, and 1.70 mg/ml, respectively. A 200-mesh copper grid (Electron Microscope Sciences, USA) was fixed with forceps. Then, 10 μL sample was dropped on the grid and left overnight to allow complete solvent evaporation. Then, 10 μL 0.5 % uranyl acetate was dropped on the grid to stain the sample. After 10 minutes, the sample was placed in the TEM for imaging.

2.3 Spectrum measurement

The excitation and emission spectra of ICG-PNIPAM nanoparticles were characterized using a spectrometer (Fluoromax-Plus-C, Horiba, Japan). The sample was first diluted 10 times with DI water, and the concentrations of PNIPAM-20mgSDS, PNIPAM-40mgSDS, PNIPAM-100mgSDS, and PNIPAM-200mgSDS were 7.9 mg/ml, 8.8 mg/ml, 8.0 mg/ml, and 8.5 mg/ml, respectively. A 300 μL quartz cuvette (Hellma, Germany) was used to hold a 200

μL diluted sample. The cuvette was placed inside a holder with stirring at 1000 rpm and temperature control at 25 °C. The emission spectrum was scanned from 575 nm to 850 nm using an excitation light of 500 nm. A 550 nm long-pass filter (Semrock, USA) was used to avoid leakage of excitation light. The excitation spectrum was scanned from 500 nm to 800 nm with a detector wavelength at 830 nm and an 825 nm long pass filter (Semrock, USA).

2.4 Fluorescence intensity study

An in-house built cuvette system was used to examine the fluorescence intensity profile over temperature [8]. A 3 mL sample was loaded into a 3.5 mL quartz cuvette and placed in a temperature-controlled holder (Quantum Northwest, Inc., USA) with a stir at 1000 rpm. An 808 nm excitation laser (MGL-II-808-2W, Dragon Lasers, China) was used to excite the sample. The emitted light from the sample passed through an 830 long-pass filter (Semrock, USA) before being collected by a modular USB spectrometer (USB2000+, Ocean Inlight, USA). The temperature measurement ranged from 30 °C to 55 °C with an increment of 0.1 °C. A temperature probe was inserted into the cuvette to monitor the sample temperature and the fluorescence intensity was recorded.

2.5 Cell culture and tumor model

Immunodeficient nude mice (female, ~25g) of strain NU/J purchased from Jackson Laboratory (USA) were used to construct subcutaneous tumor models. Pancreatic cancer cell line (BxPC-3, ATCC, USA) was cultured in Dulbecco's modified eagle's medium (DMEM, ATCC, USA). After the cell concentration reached 3×10^6 cells/mL, 100 μL solution of cells were subcutaneously injected into nude mice at the right hind flank.

2.6 Fiber bundle-based and camera-based NIR-USF imaging systems

Phantom experiments and USF imaging via local injections were performed in a previously reported fiber bundle-based USF system [11]. The excitation path consisted of a 785 nm laser (MDL-III-785-2W, Dragon Lasers, China) modulated at 1 kHz by a function generator (FG, 33220A, Agilent, USA) and a bandpass excitation filter (FF01-785/62-25, Semrock Inc., USA). Emitted fluorescence signals were collected by a fiber bundle and transmitted through two 830 nm long-pass filters (BLP01-830R, Semrock Inc., USA), a photomultiplier tube (PMT, H7422-20, Hamamatsu Photonics, Japan) driven by a high-voltage source (C8137-02, Hamamatsu, Japan) and a low-noise current preamplifier (SR570, Stanford Research Systems, USA). Finally, the emission signal was extracted by a lock-in amplifier (SR830, Stanford Research Systems, USA) with a time constant of 300ms. A FU transducer (2.5 MHz, H-108, Sonic Concepts Inc., USA) raster scanned the sample in the XY plane, and thermally enhanced fluorescence signals were recorded at each location to obtain the two-dimensional USF profile of the tube.

The USF studies via i.v. injections were conducted in a camera-based USF system that offered a high imaging sensitivity, especially in the electron-multiplying gain mode [8]. Briefly, an excitation beam from an 808 nm laser (MGL-II-808-2W, Dragon Lasers, China) passed through a bandpass filter (LL01-808-25, Semrock Inc., USA) and was split by a dual branch light guide (1/4 × 72", Edmund Optics Inc., USA) fiber into two paths to provide uniform illumination on the sample from two opposite directions. The emission light passed

through three long-pass filters (BLP01-830R-50/25, Semrock Inc., USA), a camera lens (AF NIKKOR 50 mm f/1.8D Lens, Nikon, Japan), and finally was collected by an EMCCD camera (ProEM®-HS: 1024BX3, Princeton Instruments, USA). A 2.5 MHz FU transducer (H-108, Sonic Concepts Inc., USA) powered by an amplified electrical signal from a 50 dB-gain radio frequency power amplifier (RF-AMP, A075, E&I, USA) was used to create a heated focal volume in the tissue. A three-axis motorized translation stage (XSlide™ and VXM™, Velmex Inc., USA) was used for raster scanning of the subject. During the USF experiments, the exposure time of camera was kept at 1500ms. The first fluorescence image was obtained before the FU exposure (exposure time=400 ms); the second was captured immediately after this exposure. The USF image was calculated by subtracting the corresponding pixel values of the first image from the second image, and then further filtered based on the correlation between a normalized averaging filter (typically 15 x 15 pixels) and the image (1024 x 1024 pixels).

2.7 USF imaging of a silicone tube embedded in a tissue-mimicking phantom

To simulate the blood vessel, a silicone tube (ST 60-011-02, Helix Medical, USA) with an inside diameter of 0.51 mm and an outer diameter of 0.94 mm was embedded in the silicone phantom (along the y-axis) at a depth of ~3 mm. The thickness of the phantom was 7 mm, and the method of fabricating the silicone phantom was based on a published study [9]. The absorption coefficient was estimated at 0.03 cm^{-1}, and the reduced scattering coefficient was 3.5 cm^{-1} [13]. Fig. 1(a) illustrates the schematic diagram of imaging a blood vessel-mimicking phantom sample in the fiber bundle-based USF system. The silicone tube was filled with ICG-PNIPAM and illuminated with an excitation laser beam (1.05 mW/cm^2). The mechanical index (MI) of FU was 1.72, and the exposure time was 400 ms.

2.8 USF imaging at mouse leg after a local injection

This USF study was performed in the fiber bundle-based system. About 10-15 μL contrast agent was locally injected into the hind thigh muscle of BALB/cJ mice (female, Jackson Laboratory, USA) to test the thermal responses of samples. The hair on the mice legs was shaved to avoid light scattering and provide better image contrasts. The temperature of the water bath was maintained at 37.5 °C to keep the mouse body warm. The FU transducer raster scanned a volume of 8.89 (X) * 8.89 (Y) * 3.81 (Z) mm^3 (step size in X&Y direction: 0.889 mm; step size in Z direction: 1.27 mm) with a MI value of 2.81 and exposure time of 400 ms. The excitation laser intensity was adjusted based on the fluorescence strength of each sample and had a range from 0.62 to 0.67 mW/cm^2.

2.9 *In vivo* biodistribution analysis on BxPC-3 tumor-bearing nude mice

NIR fluorescence images (λex = 808 nm, λem = 830 nm) of mice were captured at selected time points before and after an i.v. injection of 200 μL ICG-PNIPAM (n=3 for each group). For each BxPC-3 tumor bearing mouse, it was observed for the biodistribution study first for about 24 h, and USF imaging was performed afterwards. Finally, mice were euthanized at around 30 h post-administration, and their excised organs/tissues were imaged and semi-quantitatively analyzed by calculating the ratio between the average fluorescence intensity of organ and muscle.

2.10 *In vivo* NIR-USF imaging of BxPC-3 tumor via a tail vein injection

In vivo NIR-USF imaging was conducted in the camera-based USF system. Nude mice bearing BxPC-3 tumors were injected with 200 uL ICG-PNIPAM nanoparticles, and NIR fluorescence images at selected time points were captured. After acquiring the fluorescence images at 24 h post i.v. injection and a high tumor-to-background contrast was observed, the tumor-bearing mice were ready for USF imaging. The water bath temperature was kept at 37.5 °C to avoid massive heat dissipation of the mouse while it was anesthetized with 1.8 % isoflurane with a flow rate at 0.8 L/min. The scan volume was 7.62 (X) * 7.62 (Y) * 5.08 mm^3 (Z) (step size in X&Y direction: 0.762 mm; step size in Z direction: 1.27 mm). The laser intensity (λex = 808 nm) was 7.56 mW/cm^2. The acoustic pressure amplitudes of FU were adjusted based on the size and location of tumors in the mice in each USF experiment, because the acoustic energy was more attenuated in the denser tissue and longer transmission path. When a tumor was directly accessible by the ultrasound beam, the MI value was 3.63. It was adjusted up to 8.19 for one tumor when the ultrasound beam had to pass through the mouse body before reaching the tumor. In addition, these MIs were calculated based on the pressure amplitudes of FU measured via a fiber-optic hydrophone (FOHS, precision acoustic, UK) in degassed water instead of real tissues or tissue-mimicking materials. The real MI in tumors might be much lower than these numbers because of ultrasound attenuation caused by the reflection from the interface between tissue and water, and the absorption and scattering from the tissue were ignored in the calculation. Fig. 1(b) shows the experimental configuration when carrying out the *in vivo* USF imaging of mice tumor.

3 Results and discussion

3.1 Size, zeta potential, and spectrum

The size of PNIPAM nanoparticles was characterized and summarized in Fig. 2. As shown in Fig. 2(a), we have precisely controlled the hydrodynamic size of PNIPAM nanoparticles from 58 nm to 321 nm by adjusting the quantity of SDS. The hydrodynamic size of PNIPAM decreased as the quantity of SDS increased. This result agreed with the conclusion drawn by Mirja that they were able to show that different concentrations of SDS can result in a size change from 80 nm to 400 nm [14]. The polydispersity index (PDI) measures the heterogeneity of a sample based on size. A particle solution, such as lipid-based carriers, with a PDI < 0.3 was considered acceptable in drug delivery applications [15].

The capability to control the size of PNIPAM nanoparticles is critical because different sizes of PNIPAM nanoparticles can be used for various applications. The large-sized PNIPAM nanoparticles have the potential to be developed into biomarkers where the movement of the contrast agent needs to be minimized because it is more difficult to cause displacement of larger particles than smaller ones. Tumor-targeted USF imaging is desirable because it will enable future research in tumor identification, tracking, and treatment. Smaller (< 200 nm) nanoparticles may be more efficient at reaching a specific site via the EPR effect [16].

Fig. 2(b) summarizes the zeta potential of ICG-PNIPAM nanoparticles synthesized with 20, 40, 100, and 200 mg of SDS as 6.98 ± 1.34, −1.14 ± 0.84, −1.51 ± 0.67, and −3.53 ±

1.02 mV, respectively. The net surface charge of ICG-PNIPAM nanoparticles was slightly affected by the SDS quantity. As the size increased (i.e., SDS decreased), the net surface charge became more positive. This slight positive charge on the 20-mg-SDS agent is beneficial for keeping nanoparticles from aggregation and enhancing penetration through the plasma membrane [17]. Smaller-sized ICG-PNIPAM nanoparticles tended to have a slightly negative or neutral net surface charge. This is not preferred because aggregation might occur and affect the USF imaging capability. In our previous study we observed that ICG-PNIPAM-20mgSDS nanoparticles can be stored for more than 200 days [9]. Figs. 2(c) and 2(d) show the excitation and emission spectra, respectively. The excitation peak of ICG-PNIPAM was at 671 nm, and the emission peak of ICG-PNIPAM was at 605 nm, which was shifted from the 810 nm of the ICG emission peak [9]. Oxidation and denaturing of ICG dyes might occur during the synthesis of ICG-PNIPAM. The size of ICG-PNIPAM nanoparticles seldom affects on the emission spectra. In contrast, the excitation spectra of ICG-PNIPAM nanoparticles with larger sizes (e.g., 200-300 nm for PNIPAM-20mgSDS and PNIAPM-40mgSDS) were slightly broader compared to that of PNIPAM nanoparticles in smaller sizes (e.g., 50-70 nm for PNIPAM-100mgSDS and PNIPAM-200mgSDS).

The TEM images of ICG-PNIPAM nanoparticles in different sizes are displayed in Fig. 2(e), and the majority of nanoparticles are shown as a round shape. In addition, by observing the flow of ICG-PNIPAM nanoparticles suspension, we found that the viscosity of the solution increased when the SDS quantity decreased.

3.2 Fluorescence intensity profiles as a function of temperature

The relationship between the fluorescence intensity and temperature, or fluorescence profile, of ICG-PNIPAM nanoparticles in various sizes was studied, and the results are shown in Fig. 3(a). The fluorescence intensities were normalized to the strongest fluorescence emission among 4 curves. Fig. 3(b) lists vital factors, including the LCST, transition bandwidth, and ON/OFF ratio, for USF contrast agents. LCST was defined as the temperature point where the fluorescence intensity was increasing and reached 10 % of the ON/OFF fluorescence difference in the transition band, and the baseline was the average fluorescence intensity in the ‘OFF’ state. All the curves show significant increase in fluorescence intensity after the temperature is above their thresholds and obvious saturation when temperature is well above the thresholds. The curves shift along both directions in the figure, indicating that the size of the ICG-PNIPAM nanoparticles affected the fluorescence profiles. The ICG-PNIPAM had LCSTs rising from 33.8 to 37.8 °C with increased quantity of SDS, except for PNIPAM-20mgSDS. 20 mg and 100 mg SDS-mediated nanoparticles exhibited a similar background fluorescence level ('OFF' state). The PNIPAM-200mgSDS had the narrowest transition bandwidth of 6.5 °C and the highest fluorescence ON/OFF ratio of 3.38 folds. The PNIPAM-100mgSDS, and PNIPAM-200mgSDS were favored for *in vivo* applications because the switch-ON temperature thresholds were close to or slightly above body temperature. After being introduced into the body, these nanoparticles can be switched 'ON' more efficiently than those with lower temperature thresholds during USF imaging. All the nanoparticles were found to be stable and can be switched ON and OFF at least 5 times without obvious loss of the switching properties (Figs. S1(a-d)). Also, these nanoparticles exhibit stable switching properties under different biological environments such as mixing

with the bovine serum albumin (BSA) at different concentrations (Figs. S2(a-d)) and under different pH values (Figs. S2(e-h)).

3.3 USF imaging in tissue-mimic phantoms

A silicone tube was filled with ICG-PNIPAM nanoparticles of different sizes, and USF imaging was conducted to compare their performance under the same experimental conditions. The water bath temperature was maintained at body temperature using a temperature controller (PTC10, Stanford Research Systems, USA). Figs. 4(a-d) show the distributions of the four types of nanoparticles in the tube with good target-to-background contrasts. The results are similar. Briefly, the SNRs were between 24.36 and 27.16 dB, and full width at half maximum (FWHM) values varied from 1.57 to 2.00 mm as listed in Fig. 4. There were no significant differences in their USF performances when switching ON in the phantom set-up, implying no size-dependent difference in their USF performance. In this experiment, the temperature of the water bath was kept at 37.5 °C so that the USF nanoprobes with the lower LCSTs might be partially switched on already by the water bath before ultrasound exposure. This may help explain why no obvious size-dependent USF differences were observed in the tissue-mimicking phantom experiments.

3.4 USF imaging in mouse muscles via local injections

The solutions of ICG-PNIPAM nanoparticles with different sizes were respectively injected into the muscles of the hind legs of mice to evaluate the USF imaging capability. As shown in Fig. 5, the 3D distribution of the nanoparticles in each case has been successfully imaged. The interpolated USF images at 4 different depths are demonstrated in Fig. S3.

First, this indicates that the switching 'ON' property of size-varying ICG-PNIPAM probes was retained in real biological environments. Second, the volume of each USF image for PNIPAM-20mgSDS, PNIPAM-40mgSDS, PNIPAM-100mgSDS and PNIPAM-200mgSDS is 46.41, 35.51, 49.17, and 29.05 mm^3, respectively, which is much larger than the volume (~15 mm^3) of the injected nanoparticle solution in each case. This is mainly due to the transport of the nanoparticles via a convection mechanism induced by the syringe pressing. The diffusion of nanoparticles into the surrounding tissue after the injections during USF imaging may be minor due to the large size of the nanoparticles (i.e., tens to hundreds of nanometers). In addition, the transport of nanoparticles depends on the local microenvironments, and therefore the USF images show different distribution profiles in the 4 cases [18].

3.5 *In vivo* biodistribution analyses of the probes in BxPC-3 tumor-bearing nude mice

Biodistribution studies (Fig. 6) show that contrast agents dispersed throughout the mouse body immediately after an injection, and superficial vasculatures were visible. Strong fluorescence emission from the bladder appeared at one h post-injection and decreased significantly when observed at 2 h, suggesting that a portion of the nanoparticles was cleared rapidly by the renal excretion. The kidney is the primary organ responsible for renal clearance, but the hydrodynamic sizes of all proposed nanoprobes were above 58 nm, much larger than the kidney filtration threshold (6-8 nm) [19]. This is probably because contrast agents were partially dissociated into small fragments in the physiological environment and

then excreted by the renal routes. This fast renal excretion can be a favorable advantage to reduce systemic toxicity, because a fraction of nanomaterials was cleared quickly and further uptake by the reticuloendothelial system (liver and spleen) can be mitigated.

Meanwhile, the fluorescence from the spleen increased gradually with time (left-side view), and this phenomenon was especially obvious with PNIPAM-20mgSDS and PNIPAM-200mgSDS. Further analyses of harvested organs also supported the reticuloendothelial system and lungs being responsible for the uptake of most of the ICG-PNIPAM. For the PNIPAM-40mgSDS and PNIPAM-100mgSDS samples, the accumulations in the lungs were the highest. The lung serving as a biomedical filter receives not fractional, but the total cardiac output. Its pulmonary ultrastructure occupies ~25-30 % of the total endothelial surface area in the body [20], and thus there will be a high chance of nanoparticles-endothelial contacts in the vasculature of the lung. All features mentioned above facilitate the accumulation of nanoparticles in lungs. Also, such a small size of proposed nanoprobes allows for close contact with the endothelium of the mouse lung which has an average diameter of 5 μm, and nanoparticles are likely to be trapped by the ultrastructure afterwards [21]. Overall, as shown in Figs. 6 and 7, the accumulation of both nanoparticles with 20 mg and 200 mg SDS in the liver and spleen were dominant at 24 h post-injection, whereas nanoparticles synthesized with 40 mg and 100 mg SDS accumulated the most in the lungs of mice. The fluorescence images of the harvested organs and tissues at 30 h post-administration (Fig. S4) also supported this conclusion. However, while imaging organs under the 2D fluorescence camera, their volume effects cannot be neglected. For instance, the volume of the liver was the largest compared with other organs such as the spleen and lung, and the fluorescence signal was possibly biased by the volume effects because it was summed up longitudinally from a thicker volume.

The NIR fluorescence ratio between tumor and normal tissues (T/N ratio) was analyzed over a 24 h period. Fig. 8 illustrates that the T/N ratio grows with time from approximately 1.2 to 2.2 folds for all-sized ICG-PNIPAM nanoparticles. The enhanced fluorescence signals in tumors and suppressed background could be attributed to several factors. First, the emission band of ICG-PNIPAM was in the NIR band where the autofluorescence of biological tissue is low, so the background fluorescence is also relatively low. Furthermore, the prolonged circulation time is sufficient for particles to flow through tumor-associated blood vessels and then specifically retain in the tumor area via EPR effects [22]. Also, the nanoparticle concentration gradient between the vascular space and extravascular tissue may remain a high value for a long time period, which is beneficial for nanoparticles to diffuse into extravascular spaces of tumors. Figs. S5 and S6 provide the results of the biodistribution study up to 864 h, demonstrating that PNIPAM-200mg nanoprobes could remain in the tumor and reach the highest T/N ratio of 1.68 at 192 h post-injection.

It is often believed that nanoparticles with a size of 100-200 nm are good candidates for passive tumor site targeting as they are likely to escape from the filtration traps of the liver and spleen. The permeability of tumor blood vessels for large nanoparticles (>200 nm) may be limited, while small nanoprobes (<100 nm) may possibly diffuse back to the blood circulation system and comprise the tumor retention [23-24]. However, in this study, there is no dramatic variation observed in tumor accumulation for the adopted

nanoparticles. Both ICG-PNIPAM with the smallest size of 58 nm and the largest size of 321 nm demonstrated acceptable tumor-to-background ratios after 24 h as shown in Fig. 7. One possible reason could be the tumor volume differences in each mouse tumor xenograft model. Previous studies demonstrated that tumor volume affects the physiological environment and selectively changes the uptake of differently sized gold nanoparticles [24]. Size is not the only factor determining the EPR effects, and many other critical factors also exist [25]. For example, nanomaterials with a positive surface charge can be bound to the vascular endothelial cells, which leads to a rapid decrease in the concentration of free nanoparticles in the blood circulation and thus a reduction in tumor retention via the EPR mechanisms [26]. Therefore, when comparing the tumor accumulation of nanoparticles of different sizes, it is important to consider the impacts of the physiological environment and nanomaterials' chemical characteristics.

3.6 *In vivo* NIR-USF imaging of BxPC-3 tumor via a tail vein injection

Based on the results of biodistribution tests, a considerable quantity of ICG-PNIPAM could accumulate in the BxPC-3 tumor. The feasibility of conducting USF imaging in the tumor microenvironment using ICG-PNIPAM nanoparticles was examined. Figs. 9(a1-a4) show the 2D planar fluorescence images directly acquired from the camera of four tumors injected with the four different USF nanoparticles (20, 40, 100, and 200 mg SDS). The square on each figure indicates the USF scanning area and the dashed line shows the outline of the tumor. Similarly, Figs. 9(b1-b4) display their 3D USF images, indicating the distribution of USF signals (or contrast agents). Figs. 9(c1-c4) provide three slices of each 3D image in Figs. 9(b1-b4) for the four tumors. Obviously, the 2D images in Fig. 9(a) show a projection of the emission photons along the imaging direction (Z direction). Thus, fluorophores overlap axially (Z direction) and cannot be differentiated. In contrast, USF images in Figs. 9 (b-c) (and Fig. S7) clearly provide depth resolution to allow the differentiation of fluorophores along depth direction (z direction). Fig. 9(c) and Fig. S7 indicate that USF signals and agents are distributed non-uniformly on different slices. Similar results can be found on the lateral (XY) planes. In Fig. 9(a1), some USF scanning areas are not occupied by the tumor. The corresponding 3D USF images validate this result by showing strong USF signals in the tumor areas and either no signal or a weak USF signal in non-tumor areas (Figs. 9(b1), (c1) and Fig. S7 20mg). For the other three examples, although the majority of the scanning areas are in the tumors based on Figs. 9(a2-a4), their USF images show the heterogeneous distribution along both lateral (X, Y) and axial (Z) directions, which is quite different from the 2D images in Figs. 9(a2-a4) in which images are much smoother due to the light scattering and fluorescence signal overlapping. These results further indicate that USF has much higher resolution than the optical method when imaging deep tissues. Thus, the USF distribution profiles can be used to infer more detailed information on the distribution of the contrast agents in the tumor microenvironment.

All sizes of ICG-PNIPAM nanoparticles exhibited acceptable USF signals, further confirming the preferred passive accumulation of stable nanoprobes rather than free ICG molecules in the tumor sites. The successful *in vivo* USF signals also imply that the tumor microenvironments, such as hypoxia and low PH, did not dramatically affect the thermal-responsive features of proposed ICG-PNIPAM nanoparticles. The LCSTs of different-sized

nanoprobes were close to the body temperature, and contrast agents could be easily switched ‘ON’ by the FU. All the above mechanisms may be present and contribute to the in vivo USF imaging in the tumor.

Although all four nanoparticles show the successes of *in vivo* USF imaging via i.v. injections, comparisons of the USF images among the four nanoparticles should be made cautiously. Because the location and axial thickness of tumors, and therefore the applied FU power and MI are different. The MI adopted in Figs. 9(b1-b4) were 3.63, 5.57, 8.19, and 5.75, respectively. Usually, for thick tumors or tumors surrounded by thick tissues, high ultrasound power (or MI) is needed to reach good USF SNR. This is because of the ultrasound attenuation caused by unknown reflection, scattering and absorption when travelling a long distance before reaching the tumor. In this study, to reduce the imaging time all the ultrasound exposures were limited to as short as 400 ms. This is also one of the reasons that a high ultrasound power and MI were needed. Appropriately increasing the ultrasound exposure time may be an efficient way to reduce ultrasound power and MI. This will sacrifice the imaging speed and spatial resolution due to thermal diffusion. However, an ultrasound array that can simultaneously generate multiple foci combined with a Z scanning method developed in our previous publication [27] can be used to improve the temporal resolution. This method is currently being investigated in our laboratory, and preliminary data indicate a success and will be published in future.

4 Conclusions

In this paper, for the first time, we have achieved the goal of *in vivo* 3D tumor USF imaging via i.v. injections. We controlled the size of PNIPAM-based USF contrast agents by adjusting the quantity of SDS, and the average size ranged from 58 nm to 321 nm. Furthermore, we demonstrated USF imaging in both *ex vivo* blood vessel phantoms and *in vivo* mice models. Our biodistribution results showed the high contrast and passively targeted imaging of tumors possibly via EPR effects. Later, we achieved *in vivo* 3D USF imaging in the tumor with a good SNR and a tumor-to-background contrast, which is beneficial for diagnosis and therapeutic interventions, suggesting a potential high resolution tumor imaging at a depth of centimeters. Further efforts to improve this technology include developing stable and more biocompatible agents, reducing ultrasound power while retaining acceptable USF SNR, and further improving the temporal resolution of the current imaging system. All these efforts will push this technology toward adoption in pre-clinical and clinical applications for high-resolution deep-tissue fluorescence imaging.

Supplementary Material

Refer to Web version on PubMed Central for supplementary material.

Acknowledgments

This work was supported in part by funding from the NIH/NIBIB 1R15EB030809-01 (Baohong Yuan), the REP 270089 (Baohong Yuan), the CPRIT RP170564 (Baohong Yuan) and CPRIT RP210206 (Kytai T. Nguyen).

Reference

[1]. Bray F; Laversanne M; Weiderpass E; Soerjomataram I The ever-increasing importance of cancer as a leading cause of premature death worldwide. Cancer 2021, 127(16), 3029–3030. [PubMed: 34086348]

[2]. Siegel RL; Miller KD; Fuchs HE; Jemal A Cancer Statistics, 2021. CA. Cancer J. Clin 2021, 71(1), 7–33. [PubMed: 33433946]

[3]. Kosaka N; Ogawa M; Choyke PL; Kobayashi H Clinical implications of near-infrared fluorescence imaging in cancer. Future Oncol. 2009, 5(9), 1501–1511. [PubMed: 19903075]

[4]. Namikawa T; Sato T; Hanazaki K Recent advances in near-infrared fluorescence-guided imaging surgery using indocyanine green. Surg. Today 2015, 45(12), 1467–1474. [PubMed: 25820596]

[5]. Ohnishi S; Lomnes SJ; Laurence RG; Gogbashian A; Mariani G; Frangioni JV Organic Alternatives to Quantum Dots for Intraoperative Near-Infrared Fluorescent Sentinel Lymph Node Mapping. Mol. Imaging 2005, 4(3), 15353500200505128.

[6]. Schaafsma BE; Mieog JSD; Hutteman M; van der Vorst, JR; Kuppen PJK; Löwik CWGM; Frangioni JV; vande Velde CJH; Vahrmeijer AL The clinical use of indocyanine green as a near-infrared fluorescent contrast agent for image-guided oncologic surgery. J. Surg. Oncol 2011, 104(3), 323–332. [PubMed: 21495033]

[7]. Liu R; Yao T; Liu Y; Yu S; Ren L; Hong Y; Nguyen KT; Yuan B Temperature-sensitive polymeric nanogels encapsulating with β-cyclodextrin and ICG complex for high-resolution deep-tissue ultrasound-switchable fluorescence imaging. Nano Res. 2020, 13(4), 1100–1110.

[8]. Yao T; Liu Y; Ren L; Yuan B Improving sensitivity and imaging depth of ultrasound-switchable fluorescence via an EMCCD-gain-controlled system and a liposome-based contrast agent. Quant. Imaging Med. Surg 2021, 11(3), 957–968. [PubMed: 33654669]

[9]. Yu S; Cheng B; Yao T; Xu C; Nguyen KT; Hong Y; Yuan B New generation ICG-based contrast agents for ultrasound-switchable fluorescence imaging. Sci. Rep 2016, 6(1), 35942. [PubMed: 27775014]

[10]. Yu S; Yao T; Liu Y; Yuan B In vivo ultrasound-switchable fluorescence imaging using a camera-based system. Biomed. Opt. Express 2020, 11(3), 1517. [PubMed: 32206426]

[11]. Yao T; Yu S; Liu Y; Yuan B In vivo ultrasound-switchable fluorescence imaging. Sci. Rep 2019, 9(1), 9855. [PubMed: 31285475]

[12]. Liu Y; Yao T; Cai W; Yu S; Hong Y; Nguyen KT; Yuan B A Biocompatible and Near-Infrared Liposome for In Vivo Ultrasound-Switchable Fluorescence Imaging. Adv. Healthc. Mater 2020, 9(4), 1901457.

[13]. Cheng B; Bandi V; Wei M-Y; Pei Y; D'Souza F; Nguyen KT; Hong Y; Yuan B High-Resolution Ultrasound-Switchable Fluorescence Imaging in Centimeter-Deep Tissue Phantoms with High Signal-To-Noise Ratio and High Sensitivity via Novel Contrast Agents. PLoS ONE 2016, 11(11), e0165963. [PubMed: 27829050]

[14]. Andersson M; Maunu SL Structural studies of poly(N-isopropylacrylamide) microgels: Effect of SDS surfactant concentration in the microgel synthesis. J. Polym. Sci. Part B Polym. Phys 2006, 44(23), 3305–3314.

[15]. Danaei M; Dehghankhold M; Ataei S; Hasanzadeh Davarani F; Javanmard R; Dokhani A; Khorasani S; Mozafari M Impact of Particle Size and Polydispersity Index on the Clinical Applications of Lipidic Nanocarrier Systems. Pharmaceutics 2018, 10(2), 57. [PubMed: 29783687]

[16]. Acharya S; Sahoo SK PLGA nanoparticles containing various anticancer agents and tumour delivery by EPR effect. Adv. Drug Deliv. Rev 2011, 63(3), 170–183. [PubMed: 20965219]

[17]. Fröhlich E. The role of surface charge in cellular uptake and cytotoxicity of medical nanoparticles. Int. J. Nanomedicine 2012, 5577. [PubMed: 23144561]

[18]. Gehling AM; Kuszpit K; Bailey EJ; Allen-Worthington KH; Fetterer DP; Rico PJ; Bocan TM; Hofer CC Evaluation of Volume of Intramuscular Injection into the Caudal Thigh Muscles of Female and Male BALB/c Mice (Mus musculus). J. Am. Assoc. Lab. Anim. Sci. JAALAS 2018, 57(1), 35–43. [PubMed: 29402350]

[19]. Yu M; Zheng J Clearance Pathways and Tumor Targeting of Imaging Nanoparticles. ACS Nano 2015, 9(7), 6655–6674. [PubMed: 26149184]

[20]. de Wet C; Moss J METABOLIC FUNCTIONS OF THE LUNG. Anesthesiol. Clin. N. Am 1998, 16(1), 181–199.

[21]. Anselmo AC; Gupta V; Zern BJ; Pan D; Zakrewsky M; Muzykantov V; Mitragotri S Delivering Nanoparticles to Lungs while Avoiding Liver and Spleen through Adsorption on Red Blood Cells. ACS Nano 2013, 7(12), 11129–11137. [PubMed: 24182189]

[22]. Izci M; Maksoudian C; Manshian BB; Soenen SJ The Use of Alternative Strategies for Enhanced Nanoparticle Delivery to Solid Tumors. Chem. Rev 2021, 121(3), 1746–1803. [PubMed: 33445874]

[23]. Longmire M; Choyke PL; Kobayashi H Clearance Properties of Nano-sized Particles and Molecules as Imaging Agents: Considerations and Caveats. Nanomed. 2008, 3(5), 703–717.

[24]. Sykes EA; Dai Q; Sarsons CD; Chen J; Rocheleau JV; Hwang DM; Zheng G; Cramb DT; Rinker KD; Chan WCW Tailoring nanoparticle designs to target cancer based on tumor pathophysiology. Proc. Natl. Acad. Sci 2016, 113(9), E1142–E1151. [PubMed: 26884153]

[25]. Fang J; Islam W; Maeda H Exploiting the dynamics of the EPR effect and strategies to improve the therapeutic effects of nanomedicines by using EPR effect enhancers. Adv. Drug Deliv. Rev 2020, 157, 142–160. [PubMed: 32553783]

[26]. Campbell RB; Fukumura D; Brown EB; Mazzola LM; Izumi Y; Jain RK; Torchilin VP; Munn LL Cationic Charge Determines the Distribution of Liposomes between the Vascular and Extravascular Compartments of Tumors. Cancer research. 2002, 62(23), 6831–6836. [PubMed: 12460895]

[27]. Yao T; Yu S; Liu Y; Yuan B Ultrasound-Switchable Fluorescence Imaging via an EMCCD Camera and a Z-Scan Method. IEEE J. Sel. Top. Quantum Electron. 2019, 25(2), 1–8.

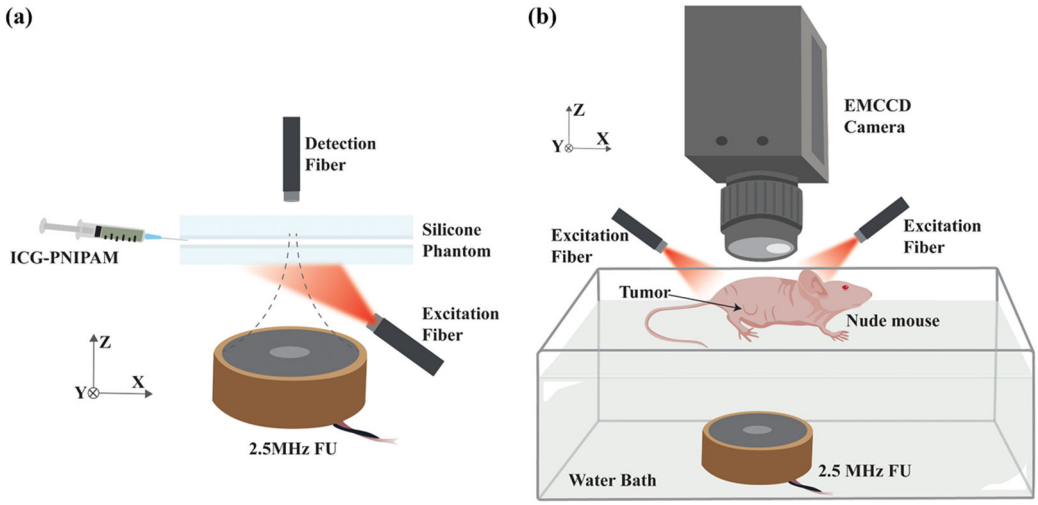

Figure 1.

The experimental set-up of USF imaging system. (a) Fiber bundle-based system: for tissue-mimicking phantom tests and (b) Camera-based system for *in vivo* USF imaging.

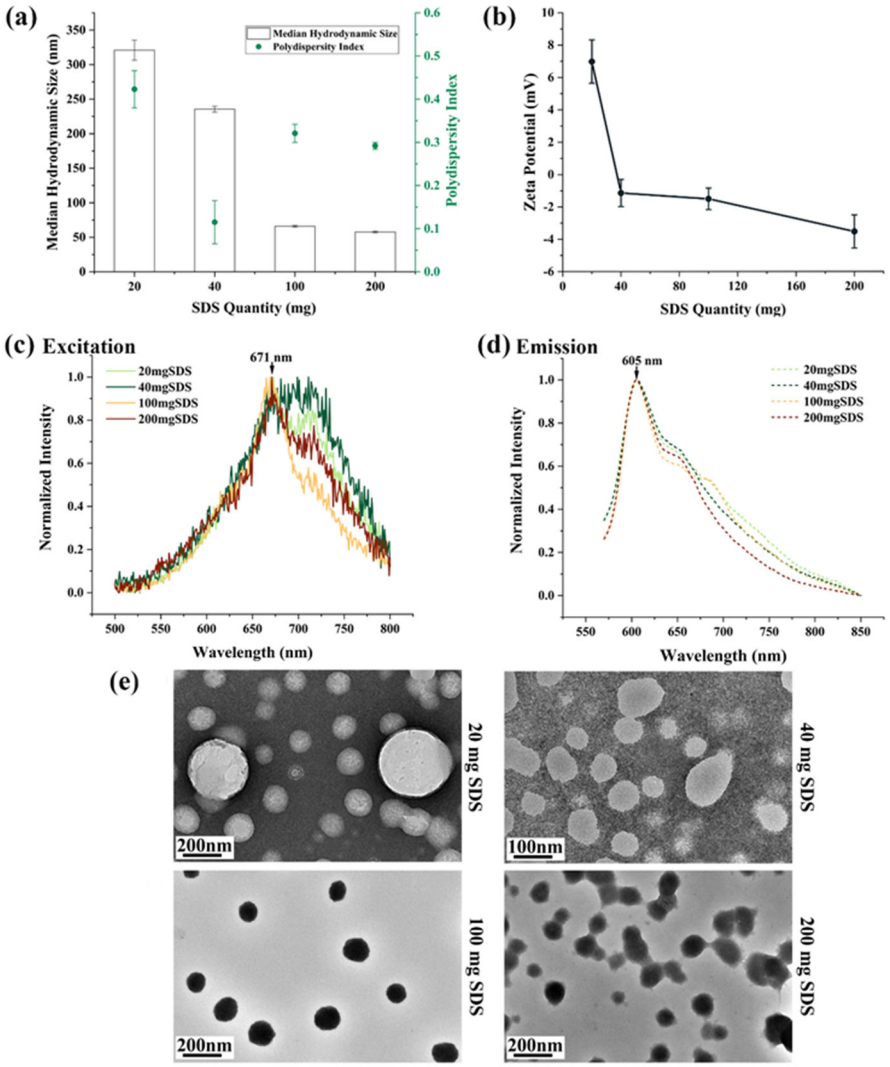

Figure 2.

Characterization of ICG-PNIPAM nanoparticles. (a) Correlation between hydrodynamic size of PNIPAM nanoparticle and the quantity of SDS (left axis); Polydispersity of PNIPAM nanoparticle synthesized with various SDS quantities (right axis). (b) Summary of zeta potential measurements for PNIPAM nanoparticles synthesized with different quantities of SDS. The number of replicas was n = 3. Normalized (c) excitation and (d) emission spectra of PNIPAM nanoparticle synthesized with various amounts of SDS. Size characterization of PNIPAM nanoparticle. The number of replicates is n > 3. (e) represents the TEM images of a single PNIPAM nanoparticle synthesized with 20, 40, 100, and 200 mg of SDS.

(a)

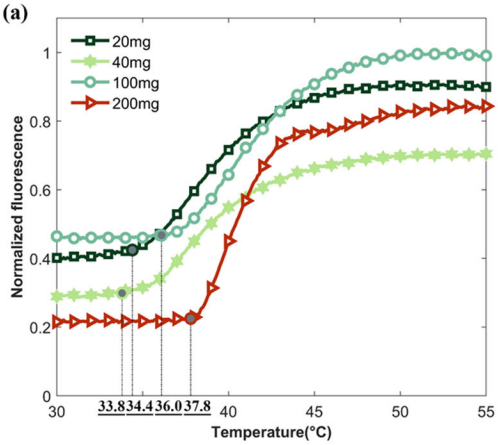

(b)

Sample	LCST (°C)	Transition Bandwidth (°C)	On/off Ratio
PNIPAM-20mgSDS	34.40	11.80	~2.07
PNIPAM-40mgSDS	33.80	12.80	~2.25
PNIPAM-100mgSDS	36.00	12.50	~2.08
PNIPAM-200mgSDS	37.80	6.50	~3.38

Figure 3.

LCST determination of PNIPAM nanoparticles. (a) Correlation between fluorescence intensity and temperature for ICG-PNIPAM nanoparticles synthesized with various quantities of SDS. (b) Detailed comparison summarized in the table.

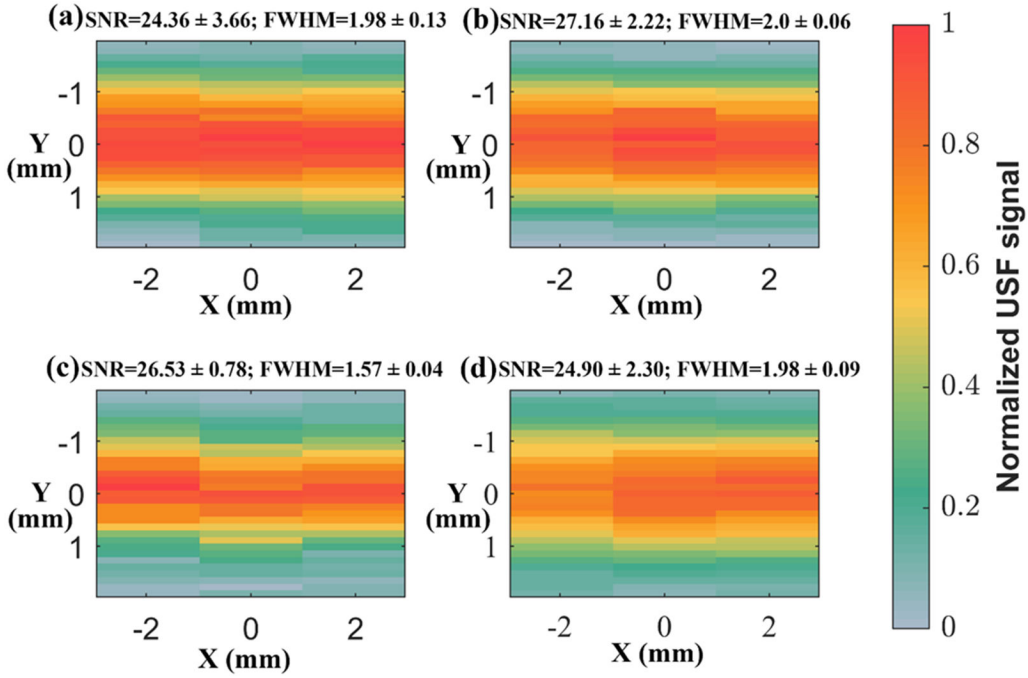

Figure 4.

The USF imaging of blood vessel-mimicking silicone phantom. Silicone tube filled with (a) 20mg SDS, (b) 40mg, (c) 100mg, and (d) 200mg SDS-mediated nanoparticles. The SNR and FWHM of each scanned USF images were also evaluated and highlighted.

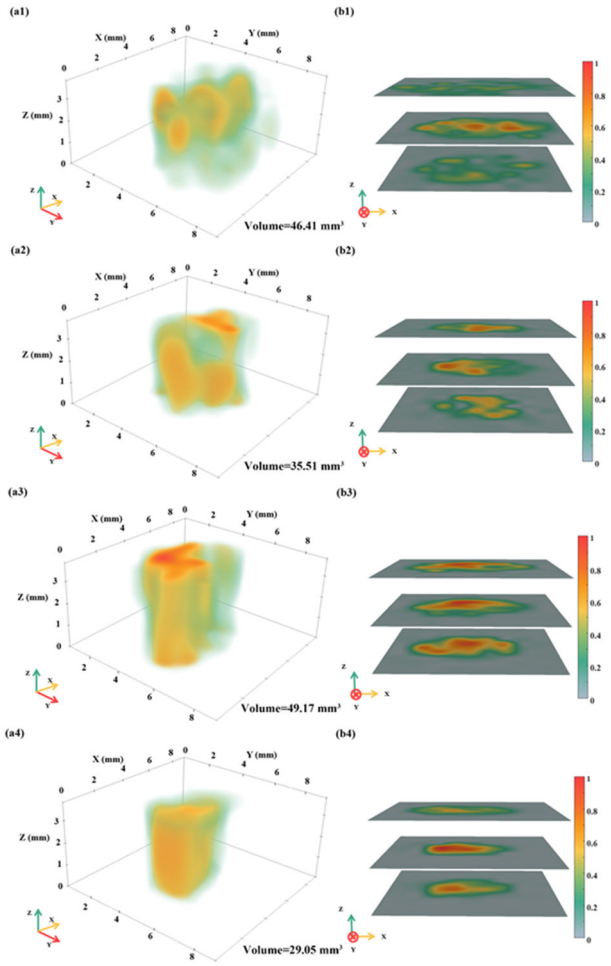

Figure 5.

(a1-4) The normalized USF images of PNIPAM-ICG-NPs distribution when locally injected into mouse leg muscle. A 30% threshold was applied when calculating the volume. (b1-4) Three stacks of 2D USF images from top, middle, and bottom layer along z axis. (a1) (b1), (a2) (b2), (a3) (b3) and (a4) (b4) are 3D reconstructed USF images for nanoparticles synthesized with 20mg, 40mg, 100mg, and 200mg SDS.

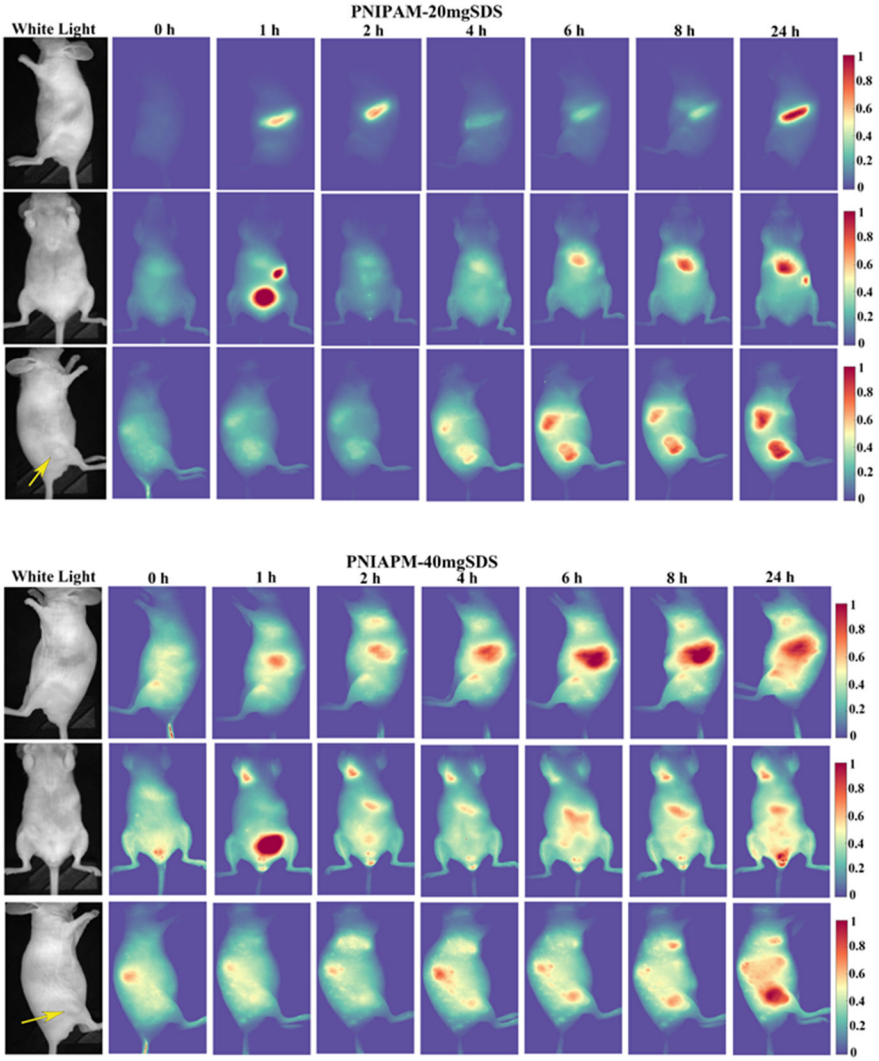

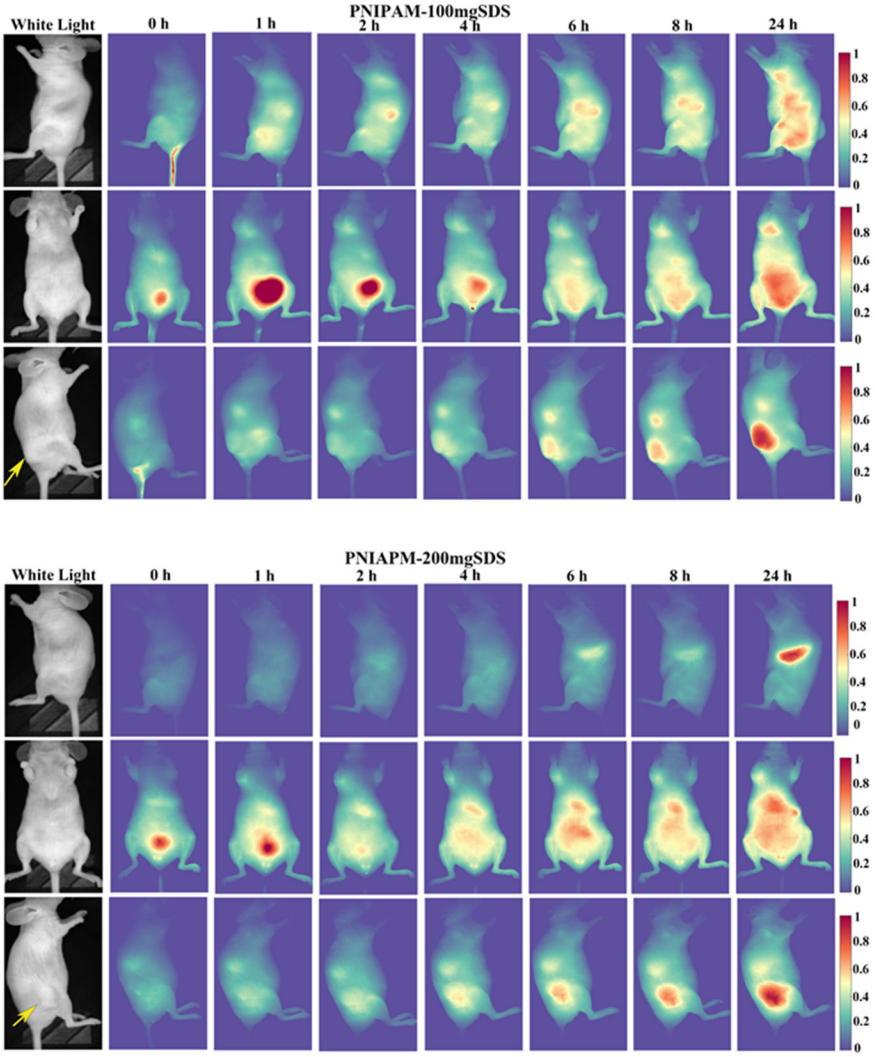

Figure 6.

The biodistribution results for PNIPAM-NPs. 2D fluorescence images captured over 24 h, including left-side view (top), ventral view (middle) and right-side view (bottom). 0 h images were acquired immediately after the i.v. injection. Tumor area is indicated by the yellow arrow.

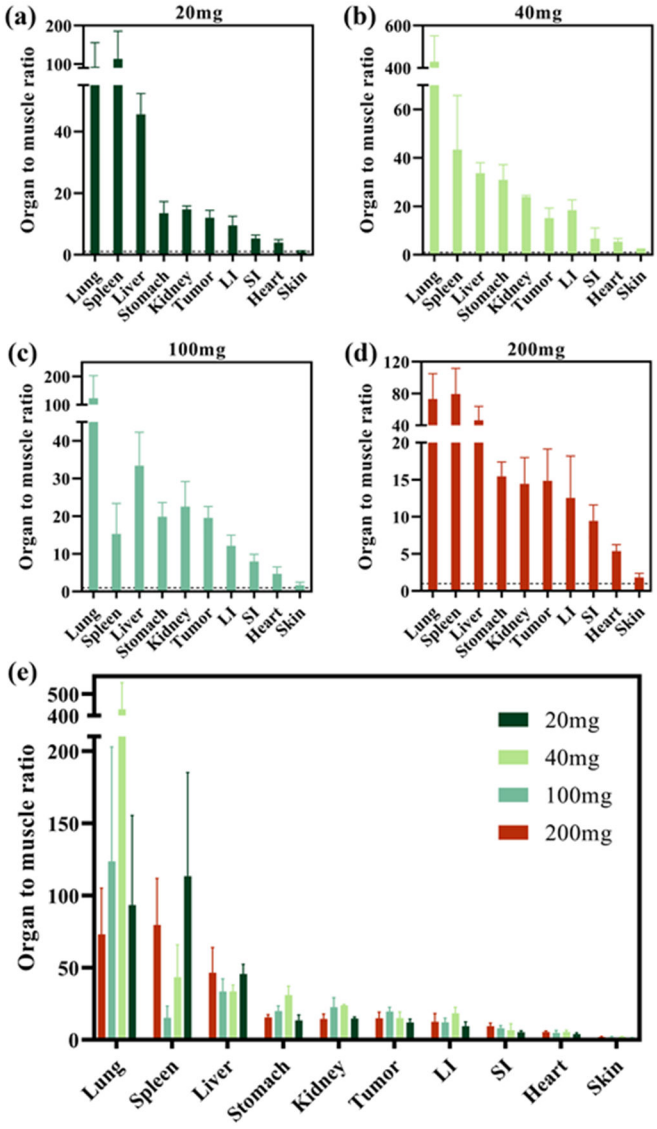

Figure 7.

The organ to muscle ratios. (a), (b), (c), and (d) correspond to PNIPAM-20mg, PNIPAM-40mg, PNIPAM-100mg and PNIPAM-200mg respectively (n = 3 for each group).LI=large intestine; SI=small intestine. The horizontal dash line at 1 represents the fluorescence level of mouse muscle.

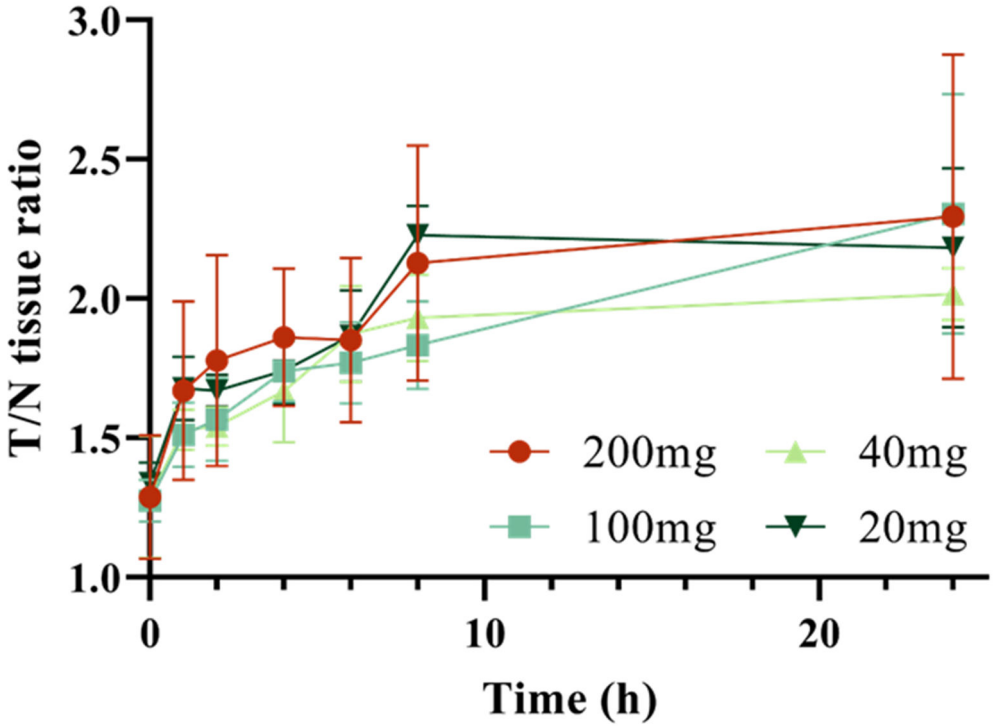

Figure 8.

The T/N ratio as a function of time after an i.v. injection of size-varying contrast agents. Data are presented as mean ± SD (n = 3).

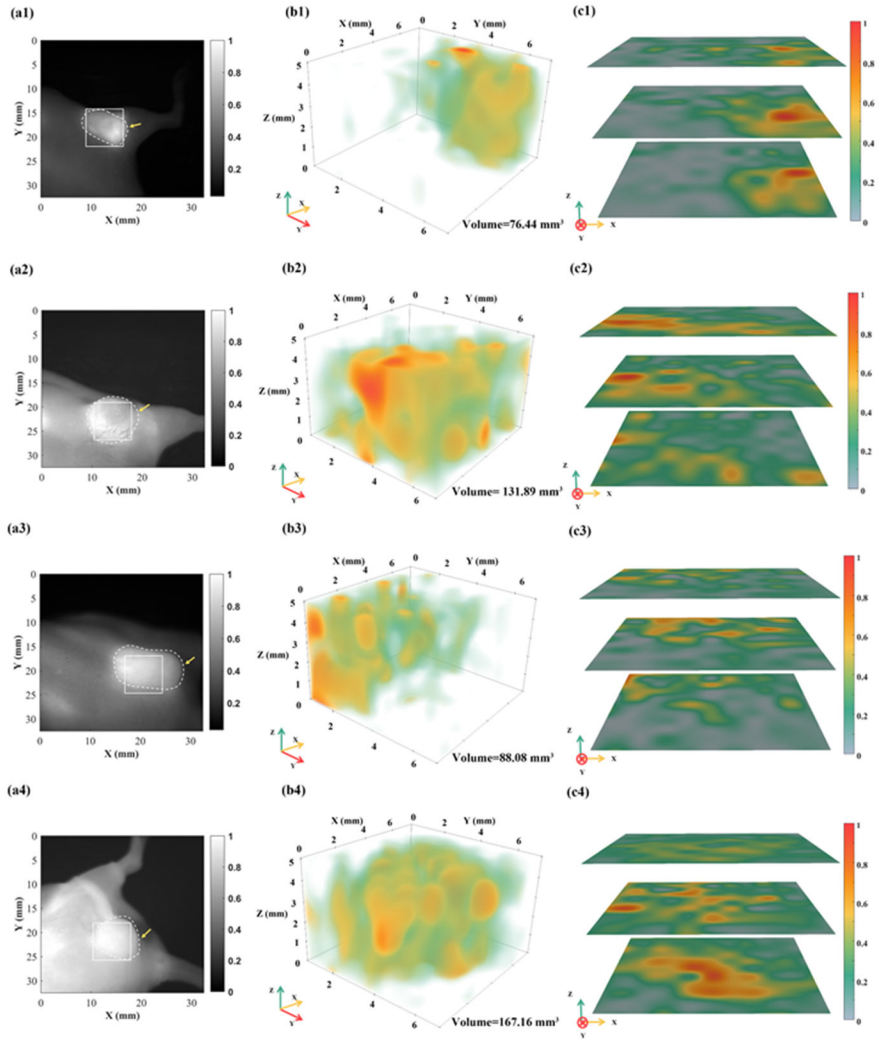

Figure 9.

(a1-4) 2D fluorescence images of the BxPC-3 pancreas tumor-bearing mouse, and the tumor area is indicated by the dashed circles and yellow arrow. Scan area is represented by the white box. (b1-4) The reconstructed 3D USF image of the tumor. Volume was calculated with a threshold of 30%. (c1-4) Three layers of 2D USF images along z axis (top, middle, and bottom). (a1)(b1)(c1), (a2)(b2)(c2), (a3)(b3)(c3), and (a4)(b4)(c4) are for contrast agents synthesized with 20mg, 40mg, 100mg, and 200mg SDS respectively.